2

A *Cacna1a* Knockin Migraine Mouse Model with Increased Susceptibility to Cortical Spreading Depression

Arn M.J.M. van den Maagdenberg,[1,2§] Daniela Pietrobon,[3§] Tommaso Pizzorusso,[4] Simon Kaja,[2,5] Ludo A.M. Broos,[1] Tiziana Cesetti,[3] Rob C.G. van de Ven,[1] Angelita Tottene,[3] Jos van der Kaa,[1] Jaap J. Plomp,[2,5] Rune R. Frants,[1] and Michel D. Ferrari [2]

[1]Department of Human Genetics, Wassenaarseweg 72, 2333 AL Leiden, The Netherlands;

[2]Department of Neurology, Leiden University Medical Centre, Wassenaarseweg 72, 2333 AL Leiden, The Netherlands;

[3]Department of Biomedical Sciences, University of Padova, CNR Institute of Neuroscience, Viale G. Colombo 3, 35121 Padova, Italy;

[4]Scuola Normale Superiore, CNR Institute of Neuroscience, Via Moruzzi 1, 56100 Pisa, Italy;

[5]Department of Neurophysiology, Leiden University Medical Centre, Wassenaarseweg 62, 2333 AL Leiden, The Netherlands;

[§]These authors contributed equally to this work.

Neuron (2004) 41: 701-710

Abstract

Migraine is a common, disabling, multifactorial, episodic neurovascular disorder of unknown etiology. Familial hemiplegic migraine type 1 (FHM1) is a Mendelian subtype of migraine with aura that is caused by missense mutations in the *CACNA1A* gene that encodes the α_1 subunit of neuronal $Ca_V2.1$ Ca^{2+} channels. We generated a knockin mouse model carrying the human pure FHM1 R192Q mutation and found multiple gain-of-function effects. These include increased $Ca_V2.1$ current density in cerebellar neurons, enhanced neurotransmission at the neuromuscular junction, and, in the intact animal, a reduced threshold and increased velocity of cortical spreading depression (CSD; the likely mechanism for the migraine aura). Our data show that the increased susceptibility for CSD and aura in migraine may be due to cortical hyperexcitability. The R192Q FHM1 mouse is a promising animal model to study migraine mechanisms and treatments.

Acknowledgements

We thank I. Hegeman and Dr. S. van Duijnen for assistance in histochemistry; E. Putignano for technical assistance; Dr. S. Verbeek for supervising the generation of chimeras; and Dr. C.L. Thompson (University of Durham, UK) for helpful discussions and advice on Western blot analysis. This work was supported by grants of the Netherlands Organisation for Scientific Research (NWO), the European Community (EC-RTN1-1999-00168), and and the Migraine Trust (to R.R.F. and/or M.D.F.); Telethon Italy, Italian Ministry of Education University Research (PRIN, FIRB, ST-L.449/97-CNR-MIUR and FISR-L. 16/10/2000-CNR-MIUR) (to D.P.); the Prinses Beatrix Fonds, the Hersenstichting Nederland, and KNAW van Leersumfonds (to J.J.P.).

Introduction

Migraine is a common, chronic neurovascular disorder, typically characterized by recurrent attacks (1–3 days) of disabling headaches and associated autonomic symptoms. In one-third of patients, attacks are accompanied by transient neurological aura symptoms (Goadsby et al., 2002). Twelve percent of the general population have on average one to two migraine attacks per month, and WHO rates migraine in the highest class of most disabling chronic disorders; treatments are frequently unsatisfactory (Goadsby et al., 2002).

The etiology of migraine is multifactorial (for reviews, see Goadsby et al., 2002; Pietrobon and Striessnig, 2003). The migraine pain is likely to be caused by activation of the trigeminovascular system, which primarily consists of trigeminal afferents innervating meningeal bloodvessels, the trigeminal nerve, and brainstem nuclei that modulate sensory signal transmission. Neuroimaging findings indicate that the migraine aura is due to cortical spreading depression (CSD), a wave of transient intense spike activity that progresses slowly along the cortex and is followed by a long-lasting neuronal suppression (Lauritzen, 1994; Cutrer et al., 1998; Hadjikhani et al., 2001; Bowyer et al., 2001). It is unknown what makes the migraine brain more susceptible to CSD.

Why and how migraine attacks begin is unknown, but CSD may play a role. CSD has been shown to activate the trigeminovascular system in animal models (Bolay et al., 2002). Alternatively, activation of certain brainstem nuclei may play an initiatory role as well (Weiller et al., 1995; Goadsby, 2001).

Familial Hemiplegic Migraine (FHM) is an autosomal-dominant subtype of migraine with aura. Apart from the characteristic hemiparesis, typical attacks of FHM are identical to those of the common forms of migraine (Thomsen et al., 2002). In addition, more than two-thirds of patients with FHM also have attacks of "normal typical migraine." This makes FHM a promising model also to study the pathogenesis of the common forms of migraine.

In over half of the families, FHM is caused by missense mutations in the *CACNA1A* gene on chromosome 19p13, FHM1 (OMIM 141500) (Joutel et al., 1993; Ophoff et al., 1994). The *CACNA1A* gene encodes the pore-forming α_1 subunit of voltage-gated neuronal $Ca_V2.1$ (P/Q-type) Ca^{2+} channels (Ophoff et al., 1996). Fifteen different missense mutations in the *CACNA1A* gene have been associated with FHM. Some mutations cause pure FHM, whereas other mutations may cause FHM plus additional neurological symptoms such as ataxia or coma (Ducros et al., 2001; Kors et al., 2002). All mutations result in substitutions of conserved amino acids in important functional regions, including the pore lining and the voltage sensors of the channel protein.

$Ca_V2.1$ channels are located throughout the mammalian nervous system (Westenbroek et al., 1995) at presynaptic terminals, where they play a prominent role in controlling neurotransmitter release (Mintz et al., 1995; Wu et al., 1999), and at somatodendritic membranes, where they also exert postsynaptic effects, such as on neuronal excitability (Pineda et al., 1998). $Ca_V2.1$ channels are expressed in all brain structures that have been implicated in the pathogenesis of migraine, including the cerebral cortex, the trigeminal ganglia, and brainstem nuclei involved in the central control of nociception (for review, see Pietrobon and Striessnig, 2003).

The functional consequences of FHM1 mutations have been investigated by expressing recombinant $Ca_V2.1$ channel subunits in heterologous systems and in cerebellar granule cells from *Cacna1a*$^{-/-}$ mice (Kraus et al., 1998; Hans et al., 1999; Tottene et al., 2002). The results, however, differed between the various expression systems, and the functional effects found in neurons were apparently contradicting: gain-of-function in single human $Ca_V2.1$ channels

(with increased Ca^{2+} influx in a broad voltage range as a consequence of their activation at lower voltages) and loss-of-function at the whole-cell level due to reduced density of functional $Ca_V2.1$ channels in the membrane (Tottene et al., 2002).

It therefore is important to study mutant $Ca_V2.1$ channels in their native neuronal environment at their endogenous level of expression when they are expressed in knockin (KI) animals. Such models will also allow evaluating the consequences of FHM1 mutations on mechanisms involved in migraine, such as neurotransmission and CSD.

Here, we generated a KI mouse model with the human R192Q pure FHM1 mutation by using a gene-targeting approach. This FHM phenotype is closest to that of the common forms of migraine. Functional analysis revealed a pure gain-of-function effect on Ca^{2+} channel current, neurotransmission, and CSD. These results may explain the underlying mechanism for the increased susceptibility of the migraine brain for CSD and aura and reinforce the hypothesis that migraine is associated with neuronal hyperexcitability at the cortical and, possibly, brainstem level.

Materials and Methods

Generation of R192Q KI Transgenic Mice

First, R192Q KI +NEO mice (see Figure 1A for details) were generated using homologous recombination in ES cells to modify the *Cacna1a* gene such that the exon 4 contained the human FHM1 R192Q mutation. Mouse genomic DNA clones were derived from a pPAC4 library (129/SvevTACfBr strain). In the targeting vector, the original CGG triplet codon 192 was changed into CAG by mutagenesis, creating the R192Q mutation. Downstream of exon 4, a PGK-driven neo cassette flanked by *Lox*P sites was present. Embryonic stem cells (E14) were electroporated, and clones were selected for homologous recombination by Southern blot analysis using external probes. The presence of the R192Q mutation was tested by PCR using primers 5′-TGTCGGGACGGAGTTTGAC-3′ and 5′-AGACTCACGCACTTGGGATT-3′ and subsequent digestion of the PCR product with the restriction enzyme *Alw*NI, as well as sequencing analysis of exon 4.

Targeted ES cells were injected into blastocysts to create chimeric animals. F1 agouti progeny were genotyped for transmission of the mutant allele, generating transgenic line R192Q KI +NEO. Heterozygous R192Q KI +NEO mice were bred with mice of the EIIA-Cre strain (Lakso et al., 1996) to remove the neo cassette. Germ line transmission was obtained and the transgenic line R192Q KI was established (Figure 1A). Mice were further bred with C57Bl/6J for five generations. Homozygous R192Q KI and wild-type (wt) littermates were used for further analysis (97% C57Bl6J background), unless stated otherwise. All animal experiments were performed in accordance with the guidelines of the respective Universities and national legislation.

RNA Analysis

Total RNA was isolated from forebrain or cerebellum using RNA Instapure (Eurogentec, Seraing, Belgium). For RT-PCR, first-strand cDNA was synthesized using random primers, and subsequent PCR was performed using *Cacna1a* and Cyclophilin specific primers (primer sequences are available from the authors upon request). PCR products of *Cacna1a* and Cyclophilin were used to probe the Northern blot using standard conditions.

Western Blot Analysis

To prevent proteolysis during the procedure, all steps were carried out on ice, and all buffers contained protease inhibitor cocktail (Cat No 1 836 170, Roche, Mannheim, Germany) and

phenylmethanesulfonyl fluoride (1 mM). Brains of the various genotypes were processed simultaneously. For the extraction of membrane proteins, whole cerebella were homogenized with a glass-Teflon homogenizer in 500 µl working solution (50 mM HEPES pH 7.4/1 mM EGTA). After a short centrifugation (5 min 20,000 rpm, Beckmann TLA 120.1), the supernatant was centrifuged for 1.5 hr at 58,000 rpm (Beckmann TLA 120.1). The membrane fractions were resuspended in 80 µl 2× Sample buffer (100 mM Tris-Glycine pH 6.8, 0.56 M β-mercaptoethanol, 2% SDS, 15% glycerol, and 0.1% BFB) and incubated for 10 min at 75°C. Protein fractions were loaded onto 4%–15% gradient SDS-PAGE.

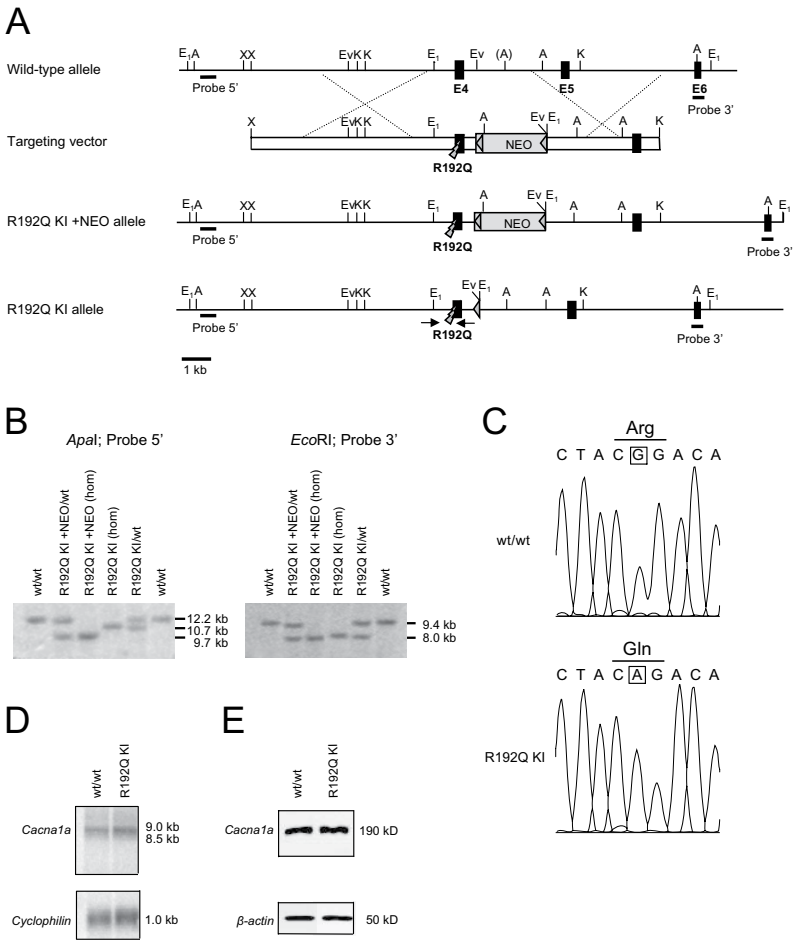

Figure 1. Generation of R192Q KI Mice.
(**A**) Relevant part of genomic structure of the wt *Cacna1a* allele, targeting vector and predicted structure after homologous recombination (R192Q KI +NEO allele), and after Cre-mediated deletion of the Neo-cassette (depicted as gray box) (R192Q KI allele). *Lox*P sites are indicated by triangles. Black boxes indicate respective exons, with the R192Q mutation in exon 4 (E4). Black horizontal lines indicate probes for Southern and Northern. Primers used for genotyping and confirmation of the R192Q mutation are depicted schematically by a pair of arrows. Restriction sites: EI, *Eco*RI; EV, *Eco*RV; K, *Kpn*I; A, *Apa*I; X, *Xba*I. (A) indicates an *Apa*I site that is polymorphic between the construct and wt allele. (**B**) Southern blot of R192Q KI +NEO and R192Q KI mutants. *Apa*I- and *Eco*RI-digested genomic DNA from three genotypes for R192Q KI +NEO and R192Q KI strains probed either the 5′ or 3′ probe. Hom: homozygote. (**C**) Sequencing analysis of RT-PCR products of cerebellar mRNA isolated from wt and homozygous R192Q KI mutant mice. (**D**) Northern blot of mRNA isolated from adult forebrain of wt and homozygous R192Q KI mice hybridized with either the *Cacna1a* or the Cyclophilin cDNA probe. (**E**) Semiquantitative Western blot of cerebellar membrane protein extracts isolated from wt and homozygous R192Q KI mice probed with $Ca_V2.1$ and actin antibody. Equal levels of $Ca_V2.1$ α_1 protein are present in wt and homozygous R192Q KI mice.

After separation, proteins were transferred onto a nitrocellulose membrane (0.2 μm). Blots were blocked with PBS/5% lowfat milk/0.05% Tween-20 and subsequently incubated o/n with primary $Ca_V2.1$ (α_1) antibody (AB5152, Chemicon, Temecula, CA) (1:200 diluted in incubation buffer [PBS/0.05% Tween-20]) together with primary actin antibody (A2066, Sigma, St Louis, MO) (1:1000 diluted in incubation buffer) at room temperature. Secondary peroxidase-labeled goat anti-rabbit antibody (Cat. nr. 111-035-003, Jackson ImmunoResearch Laboratories, West Grove, PA) (1:1000 diluted in incubation buffer) incubation was performed for 1 hr at room temperature. Western blotting was done according to the enhanced chemiluminescence ECL protocols (Amersham). Semiquantification was based on equal β-actin signal intensity.

Histology

Brains from adult mice (3 months old) were fixed in 4% PFA for 2 hr. Paraffin sections (5 μm) were prepared and stained with Klüver-Barrera staining using standard protocols.

Immunohistochemistry

Brains of adult mice (3 months old) were obtained after perfusion with PBS followed by 4% PFA fixation. Postfixation was done for 1 to 2 hr in 4% PFA followed by o/n incubation in 10% sucrose/0.1 M phosphate buffer at 4°C. Subsequently, membranes were removed, tissue was embedded in 10% sucrose/11% gelatine, and gelatin was fixed with 30% sucrose/10% formaline for 2.5 hr at room temperature, followed by o/n incubation in 30% sucrose/0.1 M phosphate buffer at 4°C. After freezing down, coronal sections of 40 μm were processed free floating during whole procedure. For immunohistochemistry, antigen retrieval was performed for 30 min at 80°C in 10 mM citrate buffer (pH 5.5). Sections were incubated in 10% heat-inactivated FCS/0.5%TX100/TBS for 2 hr and then incubated with primary $Ca_V2.1$ α_1 antibody (#ACC-001, Alomone Labs, Jerusalem, Israel) (1:200 diluted in 2% heat-inactivated FCS/0.4%TX100/TBS at 4°C). Secondary biotin-labeled goat anti-rabbit antibody (Vector Laboratories, Burlingame, CA) (1:200 diluted in the same buffer) incubation was performed for 2 hr at room temperature. Finally, for detection, sections were incubated with the avidin-biotin kit (Vector Laboratories, Burlingame, CA) for 2 hr at room temperature, washed, and developed in 0.1 mg/ml diaminobenzidine with 0.005% H_2O_2.

Electrophysiology of Cerebellar Granule Cells

Cerebellar granule cells were grown in primary culture from 6-day-old mice as described (Fletcher et al., 2001). Experiments were performed on cells grown from 6 to 7 days *in vitro*. Whole-cell patch-clamp recordings were performed at room temperature as in Fletcher et al. (2001). External recording solution: 5 mM BaCl2, 148 mM tetraethylammonium (TEA)-Cl, 10 mM HEPES (pH 7.4 with TEA-OH), and 0.1 mg/ml cytochrome C. Internal solution: 100 mM Cs-methanesulfonate, 5 mM MgCl2, 30 mM HEPES, 10 mM EGTA, 4 mM ATP, 0.5 mM GTP, and 1 mM c-AMP (pH 7.4 with CsOH). Currents were sampled at 5 kHz and low-pass filtered at 1 kHz. Compensation (typically 70%) for series resistance was generally used. Current-voltage (I-V) relationships were obtained only from cells with a voltage error of <5 mV and without signs of inadequate space clamping, such as notch-like current discontinuities, slow components in the decay of capacitative currents (in response to hyperpolarizing pulses), or slow tails not fully inhibited by nimodipine. The average normalized I-V curves were multiplied by the average maximal current density obtained from all cells. I-V curves were fitted with Equation 1: $I = G\,(V - E_{rev})\,(1 + \exp((V_{1/2} - V)/k))^{-1}$, using a nonlinear regression method based on the Levenberg-Marquardt algorithm.

The liquid junction potentials were such that a value of 12 mV should be subtracted from all voltages to obtain the correct values of membrane potential in whole-cell recordings (Fletcher et al., 2001). Averages are given as mean ± SEM.

All drugs were stored as stock solutions at −20°C: 250 μM ω-conotoxin-GVIA (ω-CgTx-GVIA, Bachem, Budendorf, Switzerland) and 250 μM ω-conotoxin-MVIIC (ω-CTx-MVIIC, Bachem, Budendorf, Swizerland) in distilled water, 10 mM nimodipine (gift from Dr. Hof, Sandoz, Basel, Switzerland) in 95% ethanol.

Ex Vivo *Electrophysiological Recordings at the Neuromuscular Junction*

Mice (male and female; 20–30 g; 3 months old) were euthanized by carbon dioxide inhalation. Phrenic nerve-hemidiaphragms were dissected and mounted in standard Ringer's medium (116 mM NaCl, 4.5 mM KCl, 2 mM $CaCl_2$, 1 mM $MgSO_4$, 1 mM NaH_2PO_4, 23 mM $NaHCO_3$, 11 mM Glucose [pH 7.4]) at room temperature. In some experiments, lower $CaCl_2$ concentrations were used. Intracellular recordings of miniature endplate potentials (MEPPs, the spontaneous depolarizing events due to uniquantal ACh release) and endplate potentials (EPPs, the depolarization resulting from nerve action potential-evoked ACh release) were made at neuromuscular junctions (NMJs) at 28°C using standard microelectrode equipment, as described previously (Plomp et al., 2000). At least 30 MEPPs and EPPs were recorded at each NMJ, and at least 10 NMJs were sampled per experimental condition per mouse. Muscle action potentials, mediated by Na^+ channels, were blocked by 2.3 μM of the selective muscle Na^+ channel blocker μ-Conotoxin GIIIB (Scientific Marketing Associates, Barnet, Herts, UK). In order to record EPPs, the phrenic nerve was stimulated supramaximally at 0.3 Hz. The amplitudes of EPPs and MEPPs were normalized to −75 mV, assuming 0 mV as the reversal potential for ACh-induced current (Magleby and Stevens, 1972). The normalized EPP amplitudes were corrected for nonlinear summation according to McLachlan and Martin (1981) with an *f* value of 0.8. Quantal content, i.e., the number of ACh quanta released per nerve impulse, was calculated by dividing the normalized and corrected mean EPP amplitude by the normalized mean MEPP amplitude.

In order to assess the contribution of P-type currents on ACh release, EPPs and MEPPs were also measured in the presence of 200 nM of the P-type-selective Ca^{2+} channel blocker ω-Agatoxin-IVA (Scientific Marketing Associates, Barnet, Herts, UK) during a 45 min measuring period, following a 15 min preincubation with the toxin.

Statistical significance was assessed using paired or unpaired Student's t tests, where appropriate, on the grand mean values, with n as the number of mice tested and with 10 to 15 NMJs tested per muscle. All experiments were performed blind to the genotypes.

Cortical Spreading Depression

Mice (male and female; 20–30 g) were anesthetized with urethane (20% in saline; 6 ml/kg injected intraperitoneally).

Wt and homozygous KI mice were fed equally, and no difference in body weight was observed between the two genotypes. The mice were not fasted prior to CSD recordings. For each recording session, four littermates, two R192Q KI mutants and two wt, were analyzed; the genotypes were disclosed at the end of the recording session. Animals that were mounted on a stereotaxic apparatus were continuously monitored for adequate level of anesthesia, temperature, stable heart rate, and nociceptive reflexes during the 100–150 min duration of the experiments. To record CSD, three holes were drilled in the skull over the left hemisphere at the following coordinates (mm from bregma): (1) electrical stimulation, posterior 5 mm, lateral 3.5; (2) micropipette 1, posterior 0.7 mm, lateral 1.4; (3) micropipette 2, anterior 1.5

mm, lateral 1.2 (Figure 5A). The steady (DC) potential was recorded with glass micropipettes mounted on a computerized micromanipulator (Marzhauser, Wetzlar, Germany) 200 µm below the dural surface (tip resistance 1–2 MΩ). An Ag/AgCl electrode was placed subcutaneous above the nose. After electrode insertion, DC potential was recorded for 10 min prior to cortical stimulation. Afterward, the first electrical stimulation was delivered (10 microAmp for 100 ms) by means of a silver bipolar electrode (500 µm tip diameter, 0.8 mm intertip distance) placed on the dura. A stimulus isolator/constant current unit (WPI, Sarasota, FL) was used to generate the stimulation current. The DC potential was then recorded for 5 min. If CSD was not elicited, 100 ms long pulses of increasing intensity (20, 30, 40, 50, 60, 80, 100, 150, 200, 300, 400, 500, 600, 800 microAmp) were applied at 5 min interval until a CSD was elicited. The charge (current intensity times stimulus duration) delivered with the first stimulation activating a CSD was then taken as CSD threshold. Cortical potentials were amplified and low-pass filtered at 100 Hz (Cyberamp, Axon Instruments, Union City, CA). Signals were continuously digitized and recorded using Labview data acquisition and analysis system. To estimate CSD propagation velocity, at the end of the experiment, the distance between the recording electrodes was accurately measured using the motorized manipulator (0.1 µm step), and this value was divided by the time elapsing between the CSD onset at electrodes 1 and 2. CSD duration was measured at half-peak amplitude.

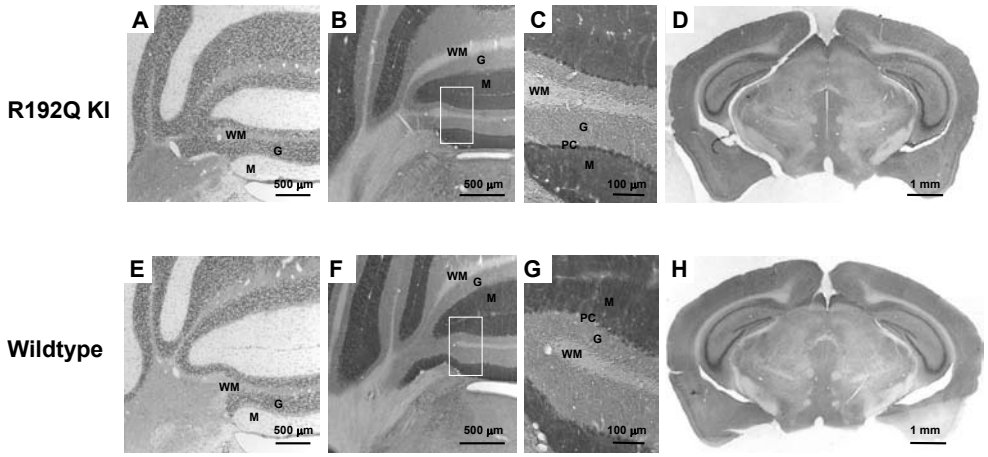

Figure 2. Histology and Expression of $Ca_V2.1$ Protein in Homozygous R192Q KI Mutants.
(**A** and **E**) Coronal sections from cerebellum of homozygous R192Q KI and wt mice stained with Klüver-Barrera. (**B** and **F**) Immunostaining of $Ca_V2.1$ α_1 protein in homozygous R192Q KI and wt cerebellum (enlarged section in [**C**] and [**G**]). (**D** and **H**) Immunostaining of $Ca_V2.1$ α_1 protein of coronal section showing a relatively high expression in the hippocampus and low overall staining in the cortical regions of homozygous R192Q KI brain. No differences in expressing level and pattern of $Ca_V2.1$ α_1 protein or apparent overall structural abnormalities were observed between both genotypes. Scale bars are depicted. WM, white matter; G, granule cell layer; M, molecular cell layer; PC, Purkinje cell layer.

Results

Generation of R192Q KI Mice

We introduced the human R192Q (FHM1) mutation at the corresponding position in the mouse ortholog *Cacna1a* gene, encoding the $Ca_V2.1$ α_1 subunit, by homologous recombination (Figure 1A). Chimeric mice were born and transmitted the R192Q KI +NEO allele through the germ line. In addition to the R192Q mutation, the mice contained the neo cassette, flanked by *Lox*P-sites. R192Q KI +NEO mice are fertile and show no overt phenotype. To delete the neo cassette, we crossed the mice with transgenic mice expressing Cre

recombinase under the control of the adenovirus EIIA early promoter (Lakso et al., 1996). Expression of Cre protein in early embryos permitted reciprocal recombination at the *Lox*P sites, resulting in removal of the neo cassette leaving only one *Lox*P site. By subsequent breeding of the heterozygous R192Q KI mice with C57Bl6J, the Cre transgene was selected against. Finally, homozygous R192Q KI mice were generated by interbreeding of R192Q KI heterozygous mice. The heterozygous and homozygous mice are viable and breed normally (data not shown). Unlike the existing natural $Ca_V2.1$ mutant mouse strains, which show a clear phenotype of epilepsy and/or ataxia (Fletcher and Frankel, 1999), the homozygous R192Q KI mice do not exhibit an overt phenotype. Correct homologous recombination in the homozygous R192Q KI mice was confirmed by Southern blot analysis (Figure 1B). Expression of mutant *Cacna1a* mRNA was shown by sequencing of RT-PCR products of cerebellar cDNA (Figure 1C) and Northern blot analysis (Figure 1D). Semiquantitative Western blot analysis, using actin as a standard, revealed equal amounts of the mutant and wt $Ca_V2.1$ α_1 protein (Figure 1E). No apparent cytoarchitectural abnormalities were observed by standard histochemical stainings in brains of homozygous R192Q KI mice (data not shown). Coronal sections of the cerebellum, with cell layers that can be distinguished with Klüver-Barrera staining (Figures 2A, E), were analyzed because of their high expression of $Ca_V2.1$ α_1 protein. Immunohistochemistry showed a normal cerebellar expression pattern for $Ca_V2.1$ α_1 protein in the homozygous R192Q KI and wt mice, with a high expression in the molecular cell layer and in Purkinje cells (Figures 2B-C, F-G). Representative coronal sections show a relatively high expression of $Ca_V2.1$ α_1 protein in the hippocampal areas and a low overall staining in, for instance, the cortical regions (Figures 2D, H).

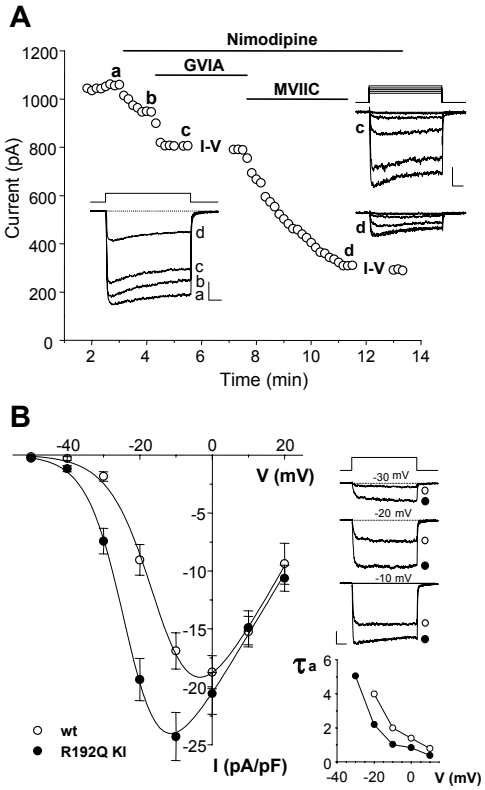

Figure 3. Increased $Ca_V2.1$ Current Density in Cerebellar Granule Cells of Homozygous R192Q KI Mice.
(**A**) Peak whole-cell Ba^{2+} current versus time recorded from a R192Q KI cerebellar granule cell during depolarizations at −10 mV every 10 s from −80 mV, before and after application of the indicated drugs. Inset: representative traces taken at times a, b, c, and d. On the right: representative traces at increasing voltage from −50 to −10 mV, taken during current-voltage (I-V) relationships measured at times c and d. Bars: 20 ms, 200 pA. $Ca_V2.1$ currents were obtained as the difference between traces at times c and d. (**B**) $Ca_V2.1$ current density, I, as a function of voltage in wt and R192Q KI granule cells. Average normalized I-V curves (n=9 for wt and n=12 for KI) were multiplied by the average maximal current density (n=27 for wt and n=39 for KI). Solid lines are fits of Equation 1 in Experimental Procedures. Inset: pooled wt and KI $Ca_V2.1$ current traces at −30, −20, and −10 mV (Bars: 20 ms, 5 pA/pF) and corresponding time constants of current activation (τ) as a function of voltage.

Gain-of-Function Effects of the R192Q Mutation on Neuronal Ca^{2+} Current

We investigated the consequences of the R192Q mutation on $Ca_V2.1$ channel function by measuring the $Ca_V2.1$ current density as a function of voltage in cerebellar granule cells in primary culture from homozygous R192Q KI and wt mice (Figure 3). To isolate the component of whole-cell Ca^{2+} current that is due to $Ca_V2.1$ channels, ω-conotoxin MVIIC (MVIIC, 3 μM), a toxin that inhibits both N- and P/Q-type calcium channels, was applied after subsequent additions of saturating concentrations of nimodipine (L-type channel blocker; 5 μM) and the specific blocker of N-type channels, ω-CgTx-GVIA (GVIA; 1 μM) (Tottene et al., 2002) (Figure 3A). This protocol enabled measurement of the L-, N-, and R-type components of the Ca^{2+} current in addition to the P/Q-type component.

The $Ca_V2.1$ current density in R192Q KI neurons was larger than in wt neurons over a broad voltage range (Figure 3B). The relative increase in R192Q KI current density was larger at lower voltages close to the threshold of channel activation and progressively diminished with increasing voltages. The voltage dependence of the relative increase in R192Q KI current density is consistent with mutant $Ca_V2.1$ channels being activated at more negative voltages than wt channels. Fitting of the current-voltage relationship curves gave half-voltage of activation values ($V_{1/2}$) of -13.9 ± 0.9 mV for the wt and of -22.7 ± 0.5 mV for the mutant channels. The kinetics of activation of the $Ca_V2.1$ current in R192Q KI neurons were faster than in wt neurons (traces and inset of Figure 3B). The shifted voltage dependence of the time constant (τ) of activation (inset of Figure 3B) is consistent with the idea that mutant channels activate at lower voltages and open more readily than wt channels.

In contrast with the finding in cerebellar granule cells isolated from *Cacna1a*$^{-/-}$ mice and transfected with mutant human $Ca_V2.1$ α_1 subunits (Tottene et al., 2002), the R192Q mutation did not decrease the density of functional $Ca_V2.1$ channels in the granule cells of the R192Q KI mouse. Given that the R192Q mutant and wt channels have identical single channel current and similar maximal open probability (Hans et al., 1999), a similar density of functional channels can be inferred from the similar $Ca_V2.1$ current densities in R192Q KI and wt granule cells at voltages higher than 0 mV (Figure 3B), where open probabilities are maximal for both mutant and wt channels (Tottene et al., 2002).

The densities of the L-, N-, and R-type components of the Ca^{2+} current were not significantly different in R192Q KI and wt granule cells: L-type, 11.3 ± 0.9 (n=30) and 13.8 ± 1.5 (n=20) pA/pF; N-type, 6 ± 0.6 (n=30) and 5.2 ± 0.6 (n=22) pA/pF; R-type, 23.7 ± 1.8 (n=39) and 23.4 ± 1.3 (n=27) pA/pF. Therefore, granule cells of the homozygous R192Q KI mice do not show alterations of other Ca^{2+} channels as a mechanism for compensation of the gain-of-function of $Ca_V2.1$ channels.

Enhanced Evoked and Spontaneous Neurotransmitter Release at the Neuromuscular Junction of R192Q KI Mice

$Ca_V2.1$ channels play a prominent role in controlling neurotransmitter release in many synapses of the mammalian nervous system. Given the fourth-power dependence of neurotransmitter release on intracellular Ca^{2+} concentration, small changes in amplitude or time course of Ca^{2+} influx at the release sites are expected to be very effective in modulating transmitter output at those synapses where the Ca^{2+} sensors are not saturated during an action potential (Schneggenburger and Neher, 2000). This predicts that at such synapses $Ca_V2.1$ channels that open more readily and at lower voltages because of the R192Q mutation lead to an increased action potential-evoked Ca^{2+} influx and a consequent increase in neurotransmitter release. To test this hypothesis, we studied neurotransmission at the neuromuscular junction (NMJ), a single synapse that shares with many central synapses the location of $Ca_V2.1$ channels at the

release sites close to the presynaptic Ca^{2+} sensors (Mintz et al., 1995; Wu et al., 1999; Urbano et al., 2003) and a similar cooperative action of Ca^{2+} ions in controlling transmitter release (Dodge and Rahamimoff, 1967; Wu and Saggau, 1997; Schneggenburger and Neher, 2000).

EPPs, representing the postsynaptic depolarizations produced by the acetylcholine (ACh) release evoked by a single action potential, were measured at both physiological concentrations of Ca^{2+} ions, probably leading to saturation of the NMJ Ca^{2+} sensors (Urbano et al., 2003) and at lower concentrations not saturating the Ca^{2+} sensors. The amount of ACh released from nerve terminals at low-rate stimulation (0.3 Hz) did not differ between genotypes when measured at 2 mM Ca^{2+} (Figure 4A) . The quantal content was 42.5 ± 1.7 and 42.6 ± 2.3 at wt (n=13, number of mice tested) and homozygous R192Q mutant (n=12) NMJs, respectively (p = 0.97). Also the kinetics of EPPs did not differ between genotypes, and the P/Q-type Ca^{2+} channel blocker ω-Agatoxin-IVA (200 nM) reduced quantal contents equally at both wt and R192Q mutant NMJs by 90% (Figures 4A, B). No differences in quantal content were found at 1 mM Ca^{2+} (Figure 4A). However, when the Ca^{2+} concentration was reduced to 0.2 mM, the quantal content was 240% higher at homozygous R192Q KI NMJs (5.0 ± 0.9 and 17.1 ± 4.1 at wt [n=7] and R192Q mutant [n=7] NMJs, respectively [p <0.05]) (Figure 4A).

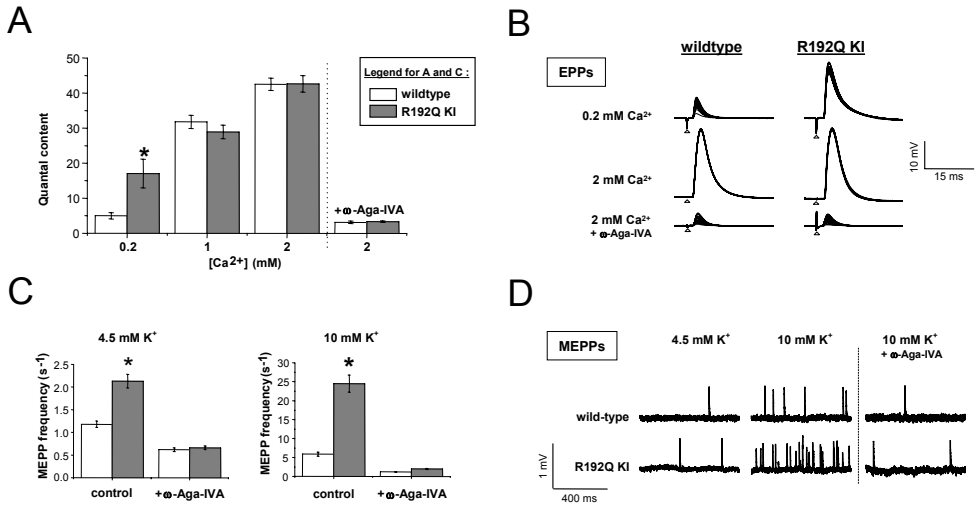

Figure 4. Increased Neurotransmitter Release at Homozygous R192Q KI Neuromuscular Synapses.
(**A**) Quantal content (upon 0.3 Hz nerve stimulation) at wt and homozygous R192Q KI neuromuscular junctions (NMJs), measured with 0.2, 1, or 2 mM Ca^{2+} in the Ringer's medium. Values obtained at 1 and 2 mM Ca2+ did not differ between genotypes. At 0.2 mM Ca^{2+}, however, the quantal content was found to be much higher at R192Q KI NMJs than at wt controls (240% increase, n=7 mice, $p < 0.05$). ω-Agatoxin-IVA (200 nM) caused a reduction of 90% on quantal content at 2 mM Ca^{2+} in both R192Q KI and wt NMJs. (**B**) Typical examples of endplate potentials (EPPs) recorded upon 0.3 Hz nerve stimulation in the different Ca^{2+} concentrations and in the presence of ω-Agatoxin-IVA (20 consecutive EPPs superimposed; the point of stimulation is indicated by arrow heads). (**C**) Spontaneous quantal ACh release was found increased by 81% at homozygous R192Q KI NMJs (n=20 mice, $p < 0.001$) compared to wt NMJs, when measured as miniature endplate potential (MEPP) frequency in normal Ringer's medium containing 4.5 mM K^+. This difference became more pronounced upon slight depolarization of nerve terminals by 10 mM K^+, increasing MEPP frequency in R192Q KI NMJs to 425% of wt controls (n=17 mice, $p < 0.001$). ω-Agatoxin-IVA greatly reduced MEPP frequency and eliminated the observed differences between the genotypes. (**D**) Typical examples of MEPPs recorded at wt and R192Q KI NMJs.
* indicates a statistically significant difference.

At the wt NMJ, $Ca_V2.1$ channels are also involved in controlling a fraction of spontaneous quantal ACh release, since the frequency of MEPPs, the spontaneous postsynaptic depolarizing events resulting from uniquantal ACh release, is sensitive to ω-Agatoxin-IVA

(Plomp et al., 2000; Figure 4C). At NMJs of homozygous R192Q KI mice, MEPP frequency was found to be increased by 81% compared to wt controls (2.13 ± 0.15 and 1.18 ± 0.07/s, respectively, $p < 0.001$, n=20, Figures 4C, D). Addition of 200 nM ω-Agatoxin-IVA reduced the MEPP frequency at wt and R192Q KI NMJs by 44% and 68% (n=10, $p < 0.001$), respectively, to almost equal values (0.62 ± 0.04 and 0.66 ± 0.04/s at wt and R192Q KI NMJs, respectively, $p = 0.53$, Figure 4C). Interestingly, in a second series of experiments, the MEPP frequency of heterozygous mice had an intermediate value (1.66 ± 0.16/s) between those of wt and homozygous R192Q KI mice (1.00 ± 0.13/s and 2.45 ± 0.30/s, respectively, n=4–6 mice, $p < 0.05$ between all three groups).

The difference in MEPP frequency between genotypes became more pronounced upon slight depolarization of nerve terminals by 10 mM K^+, increasing the MEPP frequency in homozygous R192Q KI NMJs to 425% of wt controls (24.48 ± 2.26/s (n=17) and 5.76 ± 0.53 /s (n=19) at R192Q KI and wt NMJs, respectively) (Figures 4C, D). ω-Agatoxin-IVA reduced MEPP frequency by 81% and 92% at wt and R192Q KI NMJs, respectively, to almost equal values (n=10, Figures 4C, D). Thus, the analysis of both evoked and spontaneous ACh release indicates that the R192Q FHM1 mutation leads to enhanced neurotransmission in synapses under conditions in which the synaptic Ca^{2+} sensors are not saturated. Furthermore, the intermediate synaptic phenotype of heterozygous NMJs observed with MEPP frequency, indicates an allele-dose effect, which is in accordance with dominance of the mutation in FHM patients.

Lowered Threshold and Increased Velocity for Cortical Spreading Depression in R192Q KI Mice

As mentioned earlier, CSD is the likely mechanism of migraine aura (Lauritzen, 1994; Cutrer et al., 1998; Bowyer et al., 2001; Hadjikhani et al., 2001) and can activate the trigeminovascular system in animal models (Bolay et al., 2002). Therefore, we analyzed the *in vivo* threshold for initiation, rate of propagation, and duration of CSD in anesthetized mice by electrical stimulation of the visual cortex through a bipolar electrode (Figure 5A) .

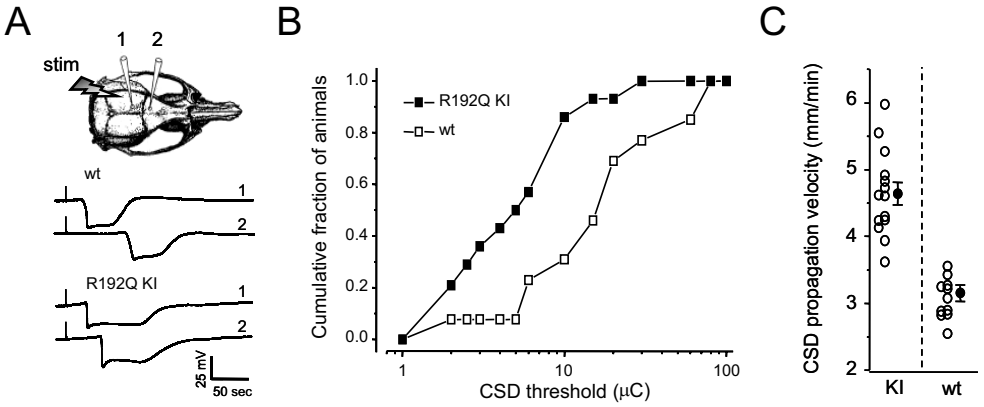

Figure 5. R192Q Mutation Facilitates the Induction and the Propagation of CSD.
(**A**) Diagram indicating location of the stimulating and recording electrodes. Examples of the CSD recordings at sites 1 and 2 are shown. Note the high velocity of propagation and the long duration of CSD in the homozygous R192Q KI mutant with respect to wt. (**B**) Cumulative distribution of CSD threshold in homozygous R192Q KI mutant (n=14) and wt (n=13) mice. The plot displays the fraction of animals showing a CSD after electrical stimulation of intensity (expressed as charge obtained from current intensity times stimulus duration) minor or equal to the corresponding value on the abscissa. The KI distribution is shifted to the left, indicating that CSD was more easily inducible in KI than in wt (Kolmogorov-Smirnov test, $p < 0.01$). (**C**) CSD propagation velocity (mm/min) is higher in homozygous R192Q KI than in wt mice (t test, $p > 0.001$). For each group, open circles represent values of single animals (n=13, wt; n=14, R192Q KI) and the filled circle represents the mean ± SEM.

The steady (DC) potential was recorded at two cortical sites located in the primary somatosensory and motor cortex. Stimulation current pulses of increasing intensity were applied at 5 min interval until a CSD was observed. The charge (current intensity times stimulus duration) delivered with the first stimulation activating a CSD was then taken as CSD threshold (Ayata et al., 2000). Homozygous R192Q KI mutants were more prone to CSD induction than their wt littermates, as significantly less charge needed to be delivered to the cortex to elicit CSD in R192Q KI mutants than in wt (7.9 ± 2.0 μC, n =14 versus 28 ± 7.6 μC, n =13, respectively; Mann-Whitney test, $p < 0.01$). A cumulative distribution of CSD threshold for the two genotypes is shown in Figure 5B.

To investigate whether the R192Q mutation affected aspects of CSD other than initiation, we also measured the velocity of CSD propagation between the two recording electrodes and CSD duration. The R192Q mutation resulted in a 150% increase of CSD velocity from 3.2 ± 0.13 mm/min in wt to 4.6 ± 0.17 mm/min in R192Q KI mutant animals (*t* test, $p < 0.001$) (Figure 5C). CSD duration was longer in R192Q KI mutants (86 ± 11 s) than in wt animals (50 ± 11 s) although this difference did not reach statistical significance (Mann-Whitney test, $p = 0.1$).

Discussion

Here, we generated the first KI transgenic mice with the pathogenic FHM1 mutation R192Q in the *Cacna1a* gene and evaluated the functional consequences for neuronal Ca^{2+} current, neurotransmission, and CSD. Our results allow several important conclusions.

First, the neuronal phenotype of the R192Q FHM1 mutation (and most likely also others) is gain-of-function in terms of Ca^{2+} influx through both single $Ca_V2.1$ channels and the whole soma as a consequence of mutant channels that open more readily and at lower voltages than wt channels. This finding considerably simplifies the picture with respect to previous findings in transfected neurons. There, a gain-of-function was found at the single channel level, but loss-of-function at the whole-cell level as a consequence of a decreased number of functional channels (Tottene et al., 2002). In light of the unchanged density of functional channels when mutant $Ca_V2.1$ channels are expressed at their endogenous level in R192Q KI neurons, the alterations in functional channel density previously found in transfected neurons (Tottene et al., 2002) and HEK293 cells (Hans et al., 1999) might have been an artifact due to overexpression. In any case, our data suggest that transfected cells (either HEK293 or neurons) are unreliable to study the consequences of ion channel mutations on the whole-cell current density. However, they can be reliably used to study the effect of mutations on the single channel function, given the similar alterations in channel gating produced by the R192Q mutation in transfected cells and KI neurons (Hans et al., 1999; Tottene et al., 2002).

Second, the gain-of-function phenotype of $Ca_V2.1$ channels was accompanied by (1) increased neurotransmission at the NMJ, in conditions where saturation of the synaptic Ca^{2+} sensors was not reached and the release probability was low (evoked release at low Ca^{2+} and spontaneous release), and (2) increased susceptibility to CSD in the intact animal, as indicated by the lowered threshold for induction and the increased velocity of propagation.

Similar to the ACh release at the NMJ, release of the neuroexcitatory amino acid glutamate from cortical neurons depends predominantly on $Ca_V2.1$ (P/Q-type) channels (Turner et al., 1992). On the other hand, $Ca_V2.1$ channels seem to play only a secondary role in controlling the cortical release of the inhibitory neurotransmitter GABA (Timmermann et al., 2002). Many brain cortical excitatory synapses are characterized by a low probability of release in

response to a single action potential (Hessler et al., 1993; Reyes et al., 1998; Schneggenburger and Neher, 2000). Our data predict an increased action potential-evoked Ca^{2+} influx at the active zones and an increased glutamate release at these synapses.

In line with this prediction is the strong decrease in intracortical glutamate concentration (with almost no change in GABA) measured by *in vivo* microdialysis during high K^+ exposure in the neocortex of the natural $Ca_V2.1$ mutant leaner mouse (Ayata et al., 2000). These mice have an electrophysiological phenotype opposite to that of the R192Q KI mutants. They carry a loss-of-function truncation mutation that shifts the channel activation curve toward less negative voltages and reduces the Ca^{2+} current density in neurons (Fletcher et al., 1996; Dove et al., 1998). In addition, *leaner* mice display a striking elevation in the threshold for initiating CSD and a slower velocity and frequent failure of propagation of CSD (Ayata et al., 2000). These data are consistent with reduced cortical network excitability in *leaner* resulting from reduced release of glutamate (with relatively unchanged GABA release). In analogy, the lowered threshold for CSD in the homozygous R192Q KI mice might be due to increased cortical network excitability resulting from increased glutamate release. Since NMDA receptor antagonists may block the initiation and propagation of CSD, glutamate is likely to be involved in both aspects of CSD (Somjen, 2001). Opposite changes in glutamate release in *leaner* and KI mice might then explain the opposite changes in velocity of propagation of CSD observed in these mutants. However, since $Ca_V2.1$ channels are located also in somatodendritic membranes throughout the brain, postsynaptic mechanisms might also contribute to the changes in the CSD threshold and rate of propagation in KI mice. In summary, our data, together with those of Ayata et al. (2000), support an important role of $Ca_V2.1$ channels in the initiation and spread of CSD and point to cortical hyperexcitability as the basis for CSD susceptibility.

Functional brain imaging and magnetoencephalography have provided evidence that migraine aura arises from CSD, and transcranial magnetic stimulation, recordings of cortical potentials, and psychophysics suggests an altered cortical excitability in migraineurs (for review, see Pietrobon and Striessnig, 2003). However, there is debate as to whether the cortex of migraineurs is hypo- or hyperexcitable and what the underlying molecular and cellular mechanisms are for the altered cortical excitability and increased susceptibility for CSD. The data from our FHM1 mouse model suggest cortical hyperexcitability due to excessive release of excitatory amino acids secondary to increased Ca^{2+} influx as the underlying mechanism in FHM.

In line with the suggested cortical hyperexcitability is also the recent observation that mutations in the ATP1A2 gene resulting in a loss of Na^+, K^+-ATPase function are associated with chromosome 1 linked FHM-2 (De Fusco et al., 2003; Vanmolkot et al., 2003). Loss of Na^+,K^+-ATPase pump function may depolarize neurons. Impaired clearance of K^+ by astrocytes, where expression of the α2 subunit of Na^+,K^+-ATPase is particularly high (Juhaszova and Blaustein, 1997), and consequent increase of extracellular K^+ may facilitate CSD.

It is generally recognized that the development of migraine headache depends on the activation of the trigeminovascular system, including trigeminal afferents innervating the meninges (for review, see Pietrobon and Striessnig, 2003). If CSD can indeed activate these afferents, as suggested by animal experiments (Bolay et al., 2002), CSD could be the trigger for migraine attacks, and FHM1 KI mice may thus provide a useful animal model for migraine. Our data predict that drugs that are capable of shifting the activation range of $Ca_V2.1$ channels to more depolarized voltages would make the cortex more resistant to CSD and may thus be able to prevent migraine attacks.

Although the consequences of FHM1 mutations on trigeminal nociception remain unexplored, one can predict that the gain-of-function synaptic FHM1 phenotype may lead to hyperexcitability of nociceptive trigeminovascular pathways due to enhanced release of vasoactive neuropeptides from perivascular nerve endings and, possibly, facilitation of sensitization of second-order central trigeminal neurons. In fact, within the trigeminovascular system, P/Q-type channels, together with N-type, control CGRP release from capsaicin-sensitive trigeminovascular afferents (Hong et al., 1999), and P/Q-type channels located in the brainstem periaquaductal gray (PAG) are involved in the descending central control of trigeminal pain perception (Knight et al., 2002). This brainstem area is of particular interest because of the apparent overlap with the site of increased metabolic activity in PET scans during migraine attacks (Weiller et al., 1995). Dysfunction of brainstem nuclei might contribute to central hyperexcitability of trigeminal pathways and consequently increased pain transmission (Goadsby et al., 2002).

In conclusion, we generated the first KI migraine mouse model and showed a pure gain-of-function effect on Ca^{2+} current, neurotransmission, and CSD. These findings support the idea of migraine as a disorder of neuronal hyperexcitability at the cortical and brainstem level. The R192Q KI mouse may provide a promising model for testing novel therapeutic strategies for migraine aimed at decreasing neuronal hyperexcitability and/or preventing CSD.